

ARTICLE INFO

Keywords:

Kinetic Alfvén waves
Plasma sheet boundary layer
Magnetospheric Multiscale (MMS)
Kinetic-scale turbulence
Spectral steepening
Collisionless dissipation
Parallel electric field
Magnetic compressibility

ABSTRACT

Energy dissipation and particle acceleration in the collisionless magnetotail plasma remain incompletely understood. While Kinetic Alfvén Waves (KAWs) are widely hypothesized to mediate these processes, observational characterization of their spectral properties and dissipation signatures in magnetotail boundary layers remains limited. We report observations of KAW turbulence and parallel electric fields (E_{\parallel}) in the outer Plasma Sheet Boundary Layer (PSBL) using high-resolution burst-mode data from the Magnetospheric Multiscale (MMS) mission. For a crossing event on May 31, 2017, we identify broadband KAW turbulence characterized by a normalized electric-to-magnetic field ratio $\mathcal{R} = |\delta E_{\parallel}|/(v_A |\delta B_{\perp}|) = 2.5 \pm 1.2$ exceeding the MHD limit, a spectral break near ion scales, a steep kinetic-range spectral slope ($\alpha = -3.48 \pm 0.13$), and low magnetic compressibility ($C_{\parallel} \approx 0.03$). We observe impulsive parallel electric field structures (up to 15 mV/m) and large-amplitude density fluctuations (up to 68%) during intervals of enhanced wave activity. The steep spectral slope, steeper than theoretical predictions for undamped KAW cascades ($-7/3$ to $-8/3$), is consistent with substantial energy removal from the cascade at kinetic scales. The near-zero correlation between the E_{\parallel} waveform and density fluctuations ($r \approx -0.03$) suggests that the observed E_{\parallel} structures are not straightforwardly organized by compressive density variations, consistent with dissipation through direct wave-particle interaction. Attribution to a specific damping channel (e.g., Landau damping) is not uniquely constrained by the present diagnostics. These observations support collisionless damping of KAW turbulence at kinetic scales in the intermediate-beta, outer PSBL of the terrestrial magnetotail.

1. Introduction

The Plasma Sheet Boundary Layer (PSBL) separates the cold, tenuous magnetotail lobes from the hot, dense central plasma sheet and is among the most dynamic regions in the terrestrial magnetosphere. Field-aligned currents, high-speed ion beams, and broadband electromagnetic fluctuations converge in this narrow transition zone, making the PSBL an important site for energy transport and conversion in the magnetotail system (Eastman, Frank, Peterson and Lennartsson, 1984; Baumjohann, Paschmann and Cattell, 1988). Understanding the microphysics of this energy transfer remains a central challenge in magnetospheric physics.

Kinetic Alfvén waves (KAWs) have emerged as a leading candidate for mediating energy transport and dissipation at kinetic scales where $k_{\perp} \rho_i \sim 1$ (Hasegawa and Chen, 1976a; Lysak and Lotko, 1996). Unlike ideal magnetohydrodynamic (MHD) Alfvén waves, KAWs develop a finite parallel electric field component E_{\parallel} through electron pressure gradients and finite ion gyroradius effects (and, where relevant, electron inertia). This E_{\parallel} enables resonant energy exchange with field-aligned electrons, commonly discussed in terms of Landau damping, and can contribute to collisionless plasma heating and particle acceleration (Wygant, Keiling, Cattell, Lysak, Temerin, Mozer, Kletzing, Scudder, Streltsov, Lotko and Russell, 2002; Chaston, Bonnell, McFadden, Carlson, Cully, Le Contel, Roux, Auster, Glassmeier, Angelopoulos and Russell, 2008).

Earlier theoretical work has predicted that finite-amplitude KAWs in intermediate-beta plasmas ($0.1 < \beta < 1$) can undergo parametric decay, transferring energy to compressive fluctuations and generating coherent structures such as density cavities (Hasegawa and Chen, 1976b; Voitenko and Goossens, 1998). Here, β is the ratio of plasma thermal pressure to magnetic pressure. The ponderomotive force associated with KAW wave packets can expel plasma from regions of high wave intensity, producing density depletions that locally modify the Alfvén speed

*Corresponding author

✉ hemam.singh@nsut.ac.in (H.D. Singh)

ORCID(s): 0009-0000-1368-9263 (M.K. Chettri); 0009-0003-3061-8944 (H.D. Singh); 0000-0003-3955-7116 (R. Mukherjee)

¹Email: mkchettri8@gmail.com

and seed further nonlinear evolution. However, the nature of daughter modes in this decay process requires careful consideration. Classical ion acoustic waves (IAWs) are most weakly damped when $T_e \gg T_i$; when $T_i/T_e > 0.1\text{--}0.2$, ion Landau damping strongly attenuates freely propagating acoustic modes (Chen, 1984). In magnetotail plasmas where $T_i/T_e \sim 1\text{--}3$ is commonly reported, compressive responses driven by finite-amplitude Alfvénic/KAW fluctuations are expected to be strongly damped and may behave as quasi-modes (density perturbations continuously driven and rapidly damped) (Terradas, Soler, Oliver and Ballester, 2022; Verscharen, Chandran, Jeong et al., 2024).

Testing whether such coupling occurs in magnetospheric plasmas requires high-resolution observations capable of resolving the relationships between KAW fields and density perturbations. The presence of correlated density structures during intervals of KAW activity would support active nonlinear coupling, whereas their absence would suggest that density variations are dominated by other boundary-layer processes. The Magnetospheric Multiscale (MMS) mission, with its high time resolution and four-spacecraft configuration, enables such measurements (Burch, Moore, Torbert and Giles, 2016). Recent MMS studies have reported KAW signatures in the magnetosheath and magnetopause (Gershman, F-Viñas, Dorelli, Boardsen, Avakov, Bellan, Schwartz, Lavraud, Coffey, Chandler, Saito, Paterson, Fuselier, Ergun, Strangeway, Russell, Giles, Pollock, Torbert and Burch, 2017; Roberts, Narita and Escoubert, 2017), documented parallel electric fields reaching tens of mV/m during substorms (Ergun, Goodrich, Stawarz, Andersson and Angelopoulos, 2015; Stawarz, Ergun and Goodrich, 2017), and presented evidence consistent with electron Landau damping in turbulent plasmas (Chen, Klein and Howes, 2019).

The same MMS event on 31 May 2017 was previously analyzed by Zhang, Yuan, Huang, Yu, Xue, Deng and Huang (2022), who focused on identifying KAWs via the frequency-dependent electric-to-magnetic field ratio, characterizing the field-aligned Poynting flux, and providing direct evidence of electron acceleration through pitch-angle distributions and parallel potential-drop estimates. That study did not characterize the turbulence spectral properties across the ion-scale break, quantify magnetic compressibility as a mode diagnostic, analyze the statistical relationship between parallel electric field structures and density fluctuations, or evaluate cadence-matched energy conversion proxies as dissipation indicators.

In this paper, we present a detailed observational analysis of a PSBL crossing on May 31, 2017. Using MMS burst-mode data and the PYSPEEDAS analysis framework (Angelopoulos, Cruce, Drozdov, Grimes, Hatziogeorgiu, King, Larson, Lewis, McTiernan, Roberts, Russell, Hori, Kasahara, Kumamoto, Matsuoka, Miyashita, Miyoshi, Shinohara, Teramoto, Faden, Halford, McCarthy, Millan, Sample, Smith, Woodger, Bonnell, Loto'aniu, Reno and Singer, 2019), we quantify KAW turbulence across the ion-scale spectral break and examine dissipation-related signatures through kinetic-range spectral scaling, magnetic compressibility, density structuring, and cadence-matched work-density proxies. These results support kinetic-scale energy conversion in the outer PSBL of Earth's magnetotail.

2. Instrumentation and Data Analysis

2.1. MMS Instrumentation

The MMS mission, launched by NASA in March 2015, comprises four identical spacecraft flying in a tetrahedral formation. This configuration enables simultaneous multipoint measurements of electromagnetic fields and plasma parameters at spatial separations down to electron kinetic scales. The MMS instrumentation suite provides the temporal resolution necessary to resolve kinetic-scale plasma dynamics (Burch et al., 2016). Our study employs high-resolution burst-mode data from the MMS-1 spacecraft, selected for its optimal data coverage during the event interval (2017-05-31, 07:21:20–07:22:10 UTC). Magnetic field measurements derive from the Fluxgate Magnetometer (FGM), which samples the DC magnetic field at 128 vectors/s in burst mode (Russell, Anderson, Baumjohann, Bromund, Dearborn, Fischer, Le, Leinweber, Leneman, Magnes, Means, Moldwin, Nakamura, Pierce, Plaschke, Rowe, Slavin, Strangeway, Torbert, Hagen, Jerber, Valavanoglou and Richter, 2016). This cadence resolves frequencies well above the local ion cyclotron frequency ($f_{ci} \approx 0.18$ Hz for the conditions reported here) while maintaining low noise floors essential for spectral analysis.

Electric field vectors are obtained from the Electric Double Probe (EDP) instrument suite, comprising the Spin-plane Double Probe (SDP) and Axial Double Probe (ADP) (Lindqvist, Olsson, Torbert, King, Granoff, Rau, Needell, Turco, Dors, Beckman, Macri, Frost, Salwen, Eriksson, Ahlen, Khotyaintsev, Porter, Lappalainen, Ergun, Wermeer and Tucker, 2016; Ergun, Tucker, Westfall, Goodrich, Malaspina, Summers, Wallace, Karlsson, Mack, Brennan, Pyber, Withnell, Torbert, Macri, Rau, Dors, Needell, Lindqvist, Olsson and Cully, 2016). In burst mode, EDP delivers three-dimensional electric field measurements at 8192 samples/s, enabling detection of high-frequency electrostatic fluctuations, solitary structures, and the parallel electric field signatures central to this investigation. Plasma moments

(density, bulk velocity, and temperature for both ions and electrons) are provided by the Fast Plasma Investigation (FPI), which delivers full sky particle distributions at 150 ms cadence for electrons and 30 ms for ions in burst mode (Pollock, Moore, Jacques, Burch, Gliese, Saito, Ombert, Avakov, Barber, Coffey, Dorelli, Gershman, Giles, Rosnack, Sber, Tucker, Westlake, Young et al., 2016).

3. Plasma Environment and Event Overview

On 2017-05-31, MMS-1 observed electromagnetic fluctuations in a boundary layer region of the magnetotail at GSE coordinates $(-20, -14, 4) R_E$. The burst-mode data for this crossing provide a continuous 80-second record from 07:21:00–07:22:20 UTC, which we use to show the full context of the encounter, including the entry into and exit from the wave-active region. For quantitative spectral estimates, we restrict the analysis to a 50-second subset (07:21:20–07:22:10 UTC) during which background conditions and fluctuation statistics are approximately stationary, as required for PSD estimation and a single power-law fit. Table 1 summarizes the plasma parameters measured during this analysis interval.

The environment is characterized by a moderate magnetic field ($B_0 = 11.5 \pm 0.5$ nT), low plasma density ($n_i = 0.15 \pm 0.03$ cm $^{-3}$), and magnetically dominated conditions ($\beta_i = 0.29$, $\beta_e = 0.12$). The relatively low ion and electron temperatures ($T_i = 0.65 \pm 0.55$ keV, $T_e = 0.27 \pm 0.10$ keV) indicate this crossing occurs in a cold transition region between the plasma sheet and tail lobes, consistent with the particle energy spectrograms in Figure 1. The large uncertainty, particularly in T_i , reflects significant temporal variability during the crossing. This ion temperature falls below the typical PSBL range of 1–5 keV, consistent with an outer-PSBL interval: the cold transition region between the hot central plasma sheet ($T_i \sim 3$ –7 keV) and the tenuous tail lobes ($T_i < 0.1$ keV; (Baumjohann et al., 1988)). The ion kinetic scales remain well-defined with $\rho_i \approx 320$ km, $d_i \approx 595$ km, and $f_{ci} \approx 0.18$ Hz, establishing the relevant scales for kinetic Alfvén wave dynamics. The electron beta satisfies $\beta_e > m_e/m_i \approx 5.4 \times 10^{-4}$, placing this plasma in the kinetic (rather than inertial) Alfvén wave regime (Lysak and Lotko, 1996).

To visualize the particle environment hosting these fluctuations, Figure 1 displays the omnidirectional differential energy flux for ions and electrons. The ion and electron temperatures reported above are obtained from MMS/FPI moment products and represent characteristic energies of the distributions, whereas the spectrogram shows how the measured flux is distributed across energy channels. The ion spectrogram (top panel) exhibits a quasi-thermal core with elevated flux primarily between 200 eV and 5 keV, with a pronounced enhancement developing in the latter half of the interval. The electron spectrogram (bottom panel) shows significant flux in the 50 eV to 1 keV range, with modulations that coincide with the wave activity described in subsequent sections. These signatures are consistent with a transition-layer plasma population and suggest local heating or acceleration on timescales comparable to the wave activity, although net energization requires detailed velocity distribution analysis.

4. Results

4.1. Wave Observations

Figure 2 presents detailed burst-mode observations of the electromagnetic fluctuations over the 80-second observation window (07:21:00–07:22:20 UTC). Panels (a) and (b) show intense, broadband fluctuations in the perpendicular electric ($|\delta E_{\perp}|$) and magnetic ($|\delta B_{\perp}|$) fields, with root-mean-square amplitudes consistent with the values in Table 1. Panel (c) reveals impulsive parallel electric field structures ($|\delta E_{\parallel}|$) with peak amplitudes reaching ~ 13 –15 mV/m. Such elevated parallel electric field amplitudes are comparable to those observed during active reconnection events, double-layer structures, and intense wave-particle interaction regions in the magnetotail (Ergun et al., 2015; Stawarz et al., 2017).

4.2. KAW Identification via Electric-to-Magnetic Field Ratio

A key diagnostic for distinguishing KAWs from ideal MHD Alfvén waves is the ratio of perpendicular electric to magnetic field fluctuations normalized by the Alfvén speed:

$$\mathcal{R} = \frac{|\delta E_{\perp}|}{v_A |\delta B_{\perp}|}. \quad (1)$$

For ideal MHD Alfvén waves, $\mathcal{R} = 1$, whereas KAWs exhibit $\mathcal{R} > 1$ due to the enhanced electric field arising from finite ion gyroradius effects at $k_{\perp} \rho_i \sim 1$ (Stasiewicz, Bellan, Chaston, Kletzing, Lysak, Maggs, Pokhotelov, Seyler,

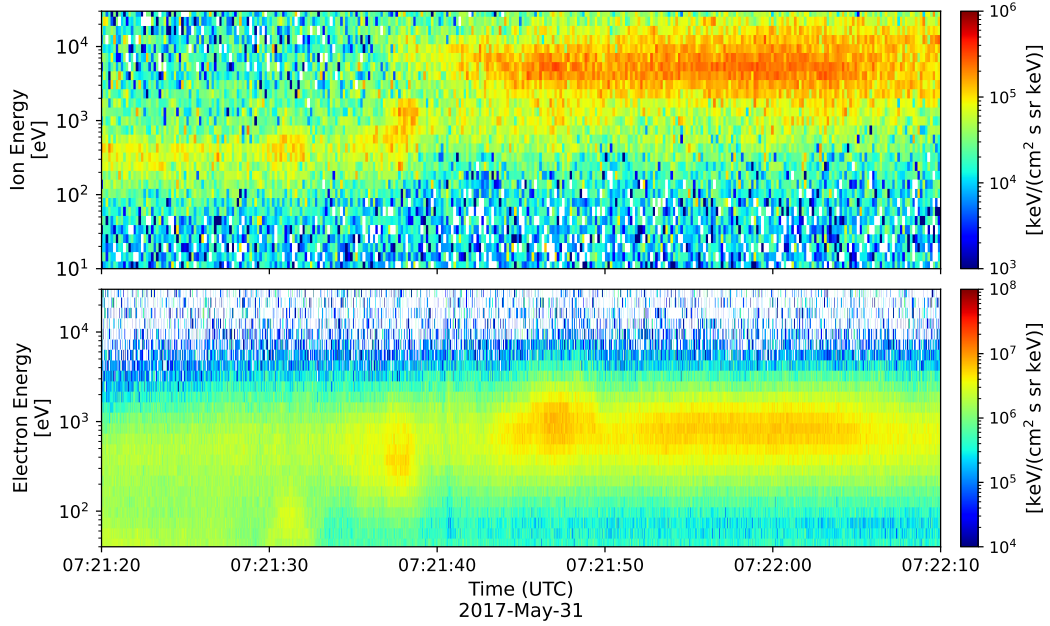
MMS-1 Energy Spectra: 07:21:20 - 07:22:10 UTC


Figure 1: Omnidirectional energy spectrograms for MMS-1 during the event interval. Top Panel: Ion energy spectrum showing a quasi-thermal population in the 0.2–5 keV range with a flux enhancement developing after 07:21:30 UTC. Bottom Panel: Electron energy spectrum showing flux variations in the 100 eV to 1 keV range. The temporal modulation of particle fluxes correlates with the interval of wave activity (07:21:20–07:22:10 UTC), consistent with local wave-particle interactions, though net energization requires detailed velocity distribution analysis.

Shukla, Stenflo, Streltsov and Wahlund, 2000; Chaston et al., 2008). As shown in Figure 2(e), the measured ratio during the analysis interval is $\mathcal{R} = 2.5 \pm 1.2$, consistently exceeding the MHD limit throughout the observation period. The scatter in this ratio reflects the turbulent, intermittent nature of the fluctuations rather than instrumental noise. This elevated ratio provides strong evidence that the observed turbulence is mediated by kinetic Alfvén waves rather than MHD modes.

4.3. Magnetic Compressibility

To further quantify the magnetic anisotropy characteristic of KAWs, we compute the magnetic compressibility as a function of frequency:

$$C_{\parallel} = \frac{|\delta B_{\parallel}|^2}{|\delta B_{total}|^2} = \frac{|\delta B_{\parallel}|^2}{|\delta B_{\parallel}|^2 + |\delta B_{\perp}|^2}. \quad (2)$$

This quantity measures the fraction of magnetic fluctuation power in the field-aligned (compressive) component. For ideal MHD Alfvén waves, $C_{\parallel} = 0$ since the fluctuations are purely transverse. Isotropic turbulence yields $C_{\parallel} = 1/3$, while compressive modes such as fast magnetosonic waves exhibit $C_{\parallel} \sim 1$. KAWs are characterized by $C_{\parallel} \lesssim 0.1$ at kinetic scales, reflecting their predominantly transverse magnetic perturbations (Gary, 1986; Sahraoui, Belmont and Goldstein, 2012).

Figure 3 presents the magnetic compressibility as a function of frequency for the analysis interval. The data reveal that the compressibility remains consistently low across the transition from MHD to kinetic scales. Within the identified KAW regime (0.18–2.0 Hz), the mean compressibility is $\langle C_{\parallel} \rangle \approx 0.029 \pm 0.008$. This value is well below both the empirical KAW threshold of 0.1 and the isotropic limit of 1/3. This persistent magnetic anisotropy ($|\delta B_{\perp}|^2 \gg |\delta B_{\parallel}|^2$) provides robust confirmation that the turbulence is mediated by shear Alfvénic fluctuations rather than compressive magnetosonic modes.

Table 1

Plasma parameters during the boundary layer crossing on 2017-05-31, 07:21:20–07:22:10 UTC. Values represent time-averaged means with standard deviations, obtained from MMS Level-2 data products (FGM magnetic field and FPI ion/electron moments) accessed via PYSPEEDAS; derived scales are computed from standard definitions.

Parameter	Symbol	Value
<i>Observational parameters</i>		
Spacecraft location (GSE)	(X, Y, Z)	$(-20, -14, 4) R_E$
Background magnetic field	B_0	11.5 ± 0.5 nT
Ion number density	n_i	0.15 ± 0.03 cm ⁻³
Ion temperature [†]	T_i	0.65 ± 0.55 keV
Electron temperature	T_e	0.27 ± 0.10 keV
Temperature ratio	T_i/T_e	2.37
Ion beta	β_i	0.29
Electron beta	β_e	0.12
Bulk ion velocity	$ \mathbf{V}_i $	~ 150 km/s
<i>Derived characteristic scales</i>		
Alfvén speed	v_A	657 km/s
Ion gyroradius	ρ_i	320 km
Ion inertial length	d_i	595 km
Ion cyclotron frequency	f_{ci}	0.18 Hz
<i>Wave properties</i>		
RMS perpendicular electric field	$\langle \delta E_{\perp}^2 \rangle^{1/2}$	1.00 mV/m
RMS perpendicular magnetic field	$\langle \delta B_{\perp}^2 \rangle^{1/2}$	0.39 nT

[†]Large uncertainty reflects significant temporal variability during the crossing.

4.4. Power Spectral Density and Spectral Break

Power spectral densities (PSDs) of magnetic and electric field fluctuations are computed using two complementary approaches. For stationary spectral characterization, we employ Welch’s method with Hanning windows and 50% overlap, yielding a frequency resolution of 0.05 Hz over the analysis interval. To resolve transient features in the time–frequency domain, we apply continuous wavelet transforms using the Morlet wavelet with nondimensional frequency $\omega_0 = 6$, providing a balance between temporal and spectral localization (Torrence and Compo, 1998). Spectral slopes in the kinetic range are determined by least-squares fitting of $\log(\text{PSD})$ versus $\log(f)$ for the perpendicular magnetic spectrum over the interval $f_{ci} < f \leq f_{\text{kaw,max}}$ (here $f_{\text{kaw,max}} = 2$ Hz). Uncertainties on spectral indices are taken from the regression standard error.

We note that the observed bulk ion velocity ($|\mathbf{V}_i| \approx 150$ km/s, $|\mathbf{V}_i|/v_A \approx 0.23$) does not satisfy the standard Taylor hypothesis condition $|\mathbf{V}_{\text{flow}}| \gg v_A$. The implications for spectral interpretation are discussed in Section 5.4.

Figure 4 summarizes the spectral properties of the field-aligned fluctuations. Panel (a) shows the magnetic-field power spectral densities in the field-aligned coordinate system, where the blue and red traces represent the perpendicular ($|\delta B_{\perp}|^2$) and parallel ($|\delta B_{\parallel}|^2$) components, respectively. A clear spectral break occurs near $f \approx 0.18$ Hz, close to the local ion cyclotron frequency (f_{ci} ; green dashed line), separating the MHD-range behavior from the sub-ion kinetic regime. For $f > f_{ci}$, the perpendicular power dominates the parallel component ($|\delta B_{\perp}|^2 \gg |\delta B_{\parallel}|^2$), demonstrating a persistent anisotropy consistent with Alfvénic/KAW turbulence and inconsistent with predominantly compressive magnetosonic fluctuations (Wygant et al., 2002; Chaston et al., 2008; Sahraoui, Goldstein, Robert and Khotyaintsev, 2009).

Panel (b) presents the electric-field spectra for the perpendicular and parallel components, δE_{\perp} and δE_{\parallel} , obtained from a Morlet-wavelet time–frequency decomposition and averaged over the analysis interval. The KAW band used throughout this study is highlighted between f_{ci} and $f_{\text{kaw,max}} = 2$ Hz (shaded region). In this band, δE_{\perp} provides the dominant contribution while a finite δE_{\parallel} is present, consistent with kinetic Alfvén wave electrodynamics and the occurrence of parallel electric-field structures discussed in Section 4.6. At frequencies above $f_{\text{kaw,max}}$, the electric-field spectra should be interpreted cautiously because projection effects, residual spin-related contamination, and increasing measurement noise can influence the apparent δE_{\parallel} level.

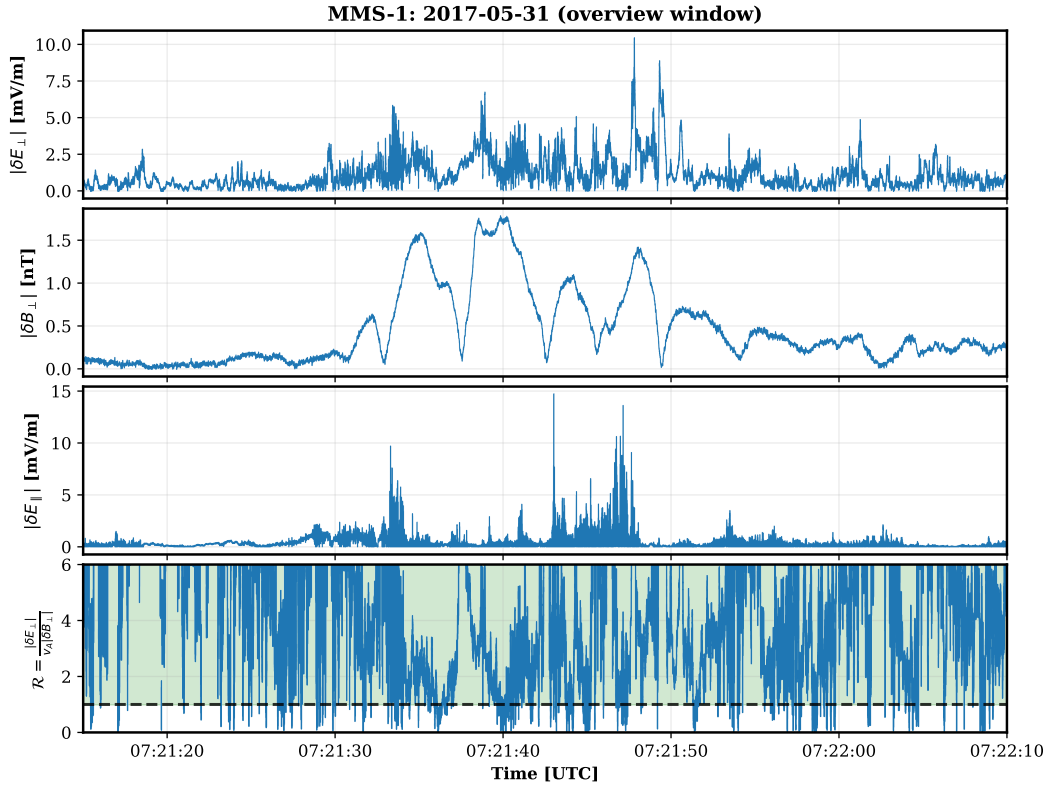


Figure 2: Overview of MMS-1 burst-mode observations during a PSBL crossing on 2017-05-31 (80-second observation window 07:21:00–07:22:20 UTC). Panels show: (a) Perpendicular electric field $|\delta E_{\perp}|$; (b) Perpendicular magnetic field $|\delta B_{\perp}|$; (c) Parallel electric field $|\delta E_{\parallel}|$ showing impulsive structures up to 13–15 mV/m; (d) Normalized ratio $|\delta E_{\perp}|/(v_A |\delta B_{\perp}|)$ (blue) with mean value 2.5 ± 1.2 , consistently exceeding the MHD limit (dashed line at unity), characteristic of KAW turbulence.

4.5. Kinetic-Range Spectral Slope

To characterize the kinetic-range cascade, we fit a power law to the *perpendicular magnetic* spectrum above f_{ci} , restricting the fit to the KAW band used in this study ($f_{ci} < f \leq f_{\text{kaw,max}} = 2$ Hz). The regression yields a spectral slope of $\alpha = -3.48 \pm 0.13$ with $R^2 = 0.97$, indicating that a single power law provides a strong description of the kinetic-range scaling over this interval. This scaling is significantly steeper than the standard Kolmogorov index ($-5/3$) characteristic of the MHD inertial range and also steeper than theoretical predictions for undamped KAW turbulence, which typically range from $-7/3 \approx -2.33$ (Boldyrev and Perez, 2012) to $-8/3 \approx -2.67$ (Howes, Cowley, Dorland, Hammett, Quataert and Schekochihin, 2008).

The steeper-than-predicted kinetic-range slope observed here is consistent with enhanced dissipation at sub-ion scales, as has been reported in other magnetospheric environments (Sahraoui et al., 2009; Huang, Sahraoui, Deng, He, Yuan, Zhou, Pang and Fu, 2014; Roberts et al., 2017) and is consistent with numerical predictions showing spectral steepening when damping is included (Chettri, Singh, Shrivastav, Singh and Mukherjee, 2025). Possible mechanisms contributing to this steepening include: (1) electron Landau damping of KAWs, which removes energy from the turbulent cascade at kinetic scales; (2) intermittency, wherein energy concentrates in localized coherent structures; and (3) enhanced dissipation in ion-scale current sheets. The combination of strong perpendicular anisotropy, the spectral break near f_{ci} , and the steep kinetic-range slope supports an interpretation of KAW turbulence undergoing significant damping. Due to the limited event duration, we do not attempt a robust characterization of the low-frequency MHD-range slope ($f < f_{ci}$).

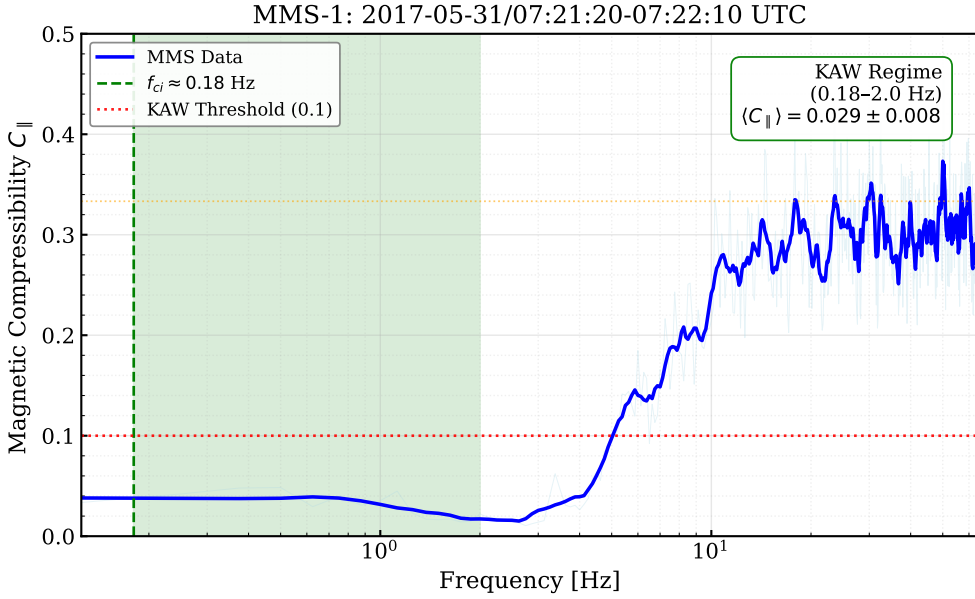


Figure 3: Frequency dependence of magnetic compressibility, defined as $C_{||} = |\delta B_{||}|^2 / |\delta B_{total}|^2$. The blue trace shows the smoothed MMS data. The vertical green dashed line marks the local ion cyclotron frequency ($f_{ci} \approx 0.18$ Hz). The horizontal red dotted line indicates the empirical upper limit for KAW identification ($C_{||} \approx 0.1$). The green shaded region highlights the kinetic range (0.18–2.0 Hz), where the observed mean compressibility is $\langle C_{||} \rangle = 0.029 \pm 0.008$. This value lies well below the 0.1 threshold, confirming the predominantly transverse nature of the magnetic fluctuations.

4.6. Parallel Electric Fields, Density Structures, and Correlation Analysis

Parallel electric fields provide a direct diagnostic of non-ideal plasma dynamics and are therefore central to assessing how electromagnetic fluctuations exchange energy with particles. In an ideal Alfvénic response one expects $E_{||} \approx 0$, whereas finite $E_{||}$ arises naturally for kinetic Alfvén waves (KAWs) and, more generally, whenever dispersive and charge-separation effects become important. Density structuring quantifies the compressive response of the plasma and may reflect either wave polarization (including KAW-associated compressibility) or independent boundary-layer and large-scale dynamics. Figure 5 is therefore used to address a specific question relevant to interpreting the interval: *do the most intense $E_{||}$ bursts show a simple linear correspondence with the contemporaneous density perturbations?*

The parallel electric field is constructed on the electric-field timeline as

$$E_{||}(t) = \mathbf{E}(t) \cdot \hat{\mathbf{b}}(t) = \frac{\mathbf{E}(t) \cdot \mathbf{B}(t)}{|\mathbf{B}(t)|}, \quad (3)$$

where \mathbf{B} is linearly interpolated to the higher-cadence electric-field timestamps before projection. The normalized density fluctuation is defined as

$$\frac{\delta n_e(t)}{n_0(t)} = \frac{n_e(t) - n_0(t)}{n_0(t)}, \quad (4)$$

with the background $n_0(t)$ obtained from an 8-s moving average of $n_e(t)$. This choice suppresses slow drifts and highlights density structure on timescales shorter than the smoothing window. For plotting, the density series is displayed on the same time axis as $E_{||}$ by interpolation; this is done to enable visual comparison and does not introduce additional information beyond the native moment cadence.

Figure 5 shows that $E_{||}$ is strongly intermittent during the interval of enhanced activity, with excursions exceeding ± 10 mV/m and peak amplitudes approaching ~ 15 mV/m (top panel). Over the same interval the density exhibits large fractional variations, with $\delta n_e/n_0$ reaching values of order $\sim +0.6$ during enhancements and ~ -0.5 during depletions (bottom panel). The temporal overlap of intense $E_{||}$ bursts with strong density structuring indicates that non-ideal fields are present while the plasma is also highly inhomogeneous; however, overlap alone does not imply that the two signals are dynamically locked.

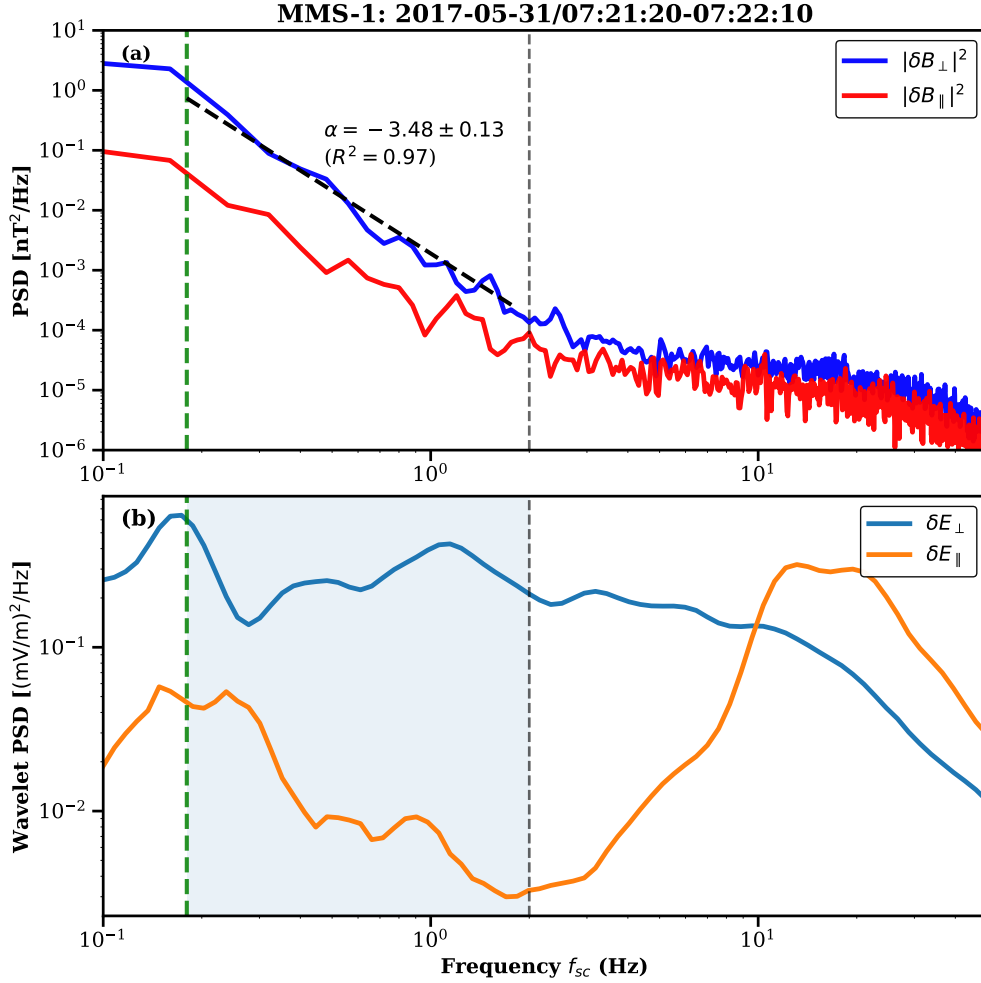


Figure 4: Two-panel power spectral density summary of field-aligned fluctuations for MMS-1 during 2017-05-31/07:21:20–07:22:10 UTC. **(a)** Magnetic-field PSDs in the field-aligned coordinate system: perpendicular $|\delta B_{\perp}|^2$ (blue) and parallel $|\delta B_{\parallel}|^2$ (red). The vertical green dashed line marks the local ion cyclotron frequency ($f_{ci} \approx 0.18$ Hz). The black dashed line denotes a power-law fit to the perpendicular magnetic spectrum in the kinetic range, yielding $\alpha = -3.48 \pm 0.13$ with $R^2 = 0.97$. The vertical gray dashed line marks the adopted upper bound of the KAW band ($f_{\text{kaw,max}} = 2$ Hz). **(b)** Electric-field spectra for δE_{\perp} and δE_{\parallel} obtained from a Morlet-wavelet time–frequency analysis and averaged over the same interval. The shaded region highlights the KAW band between f_{ci} and $f_{\text{kaw,max}}$.

To quantify their relationship within the plotted processing chain, a zero-lag Pearson correlation coefficient is computed over 07:21:30–07:21:45 UTC using the displayed $E_{\parallel}(t)$ and the smoothed $\delta n_e/n_0(t)$ placed on the same time grid. The resulting value, $r = -0.03$, indicates that within this window there is no evidence for a simple linear, zero-lag association between the instantaneous signed E_{\parallel} waveform and the background-removed density fluctuation defined by the adopted $n_0(t)$. This argues against an interpretation in which the largest E_{\parallel} spikes are merely proportional to the large-scale density enhancement/depletion captured by the 8-s background. Instead, the intermittency in E_{\parallel} is consistent with localized non-ideal structure and/or dispersive dynamics that need not track the moment-scale density variations.

It is emphasized that $r \simeq 0$ is a statement about *linear, zero-lag* association under the specific filtering and time-base choices, and it does not exclude time-lagged coupling, nonlinear dependence, or scale-dependent relationships. Within these limitations, the analysis supports the conservative conclusion that the observed parallel-field bursts are not straightforwardly explained by the large-amplitude density structuring alone, motivating further diagnostics (e.g.,

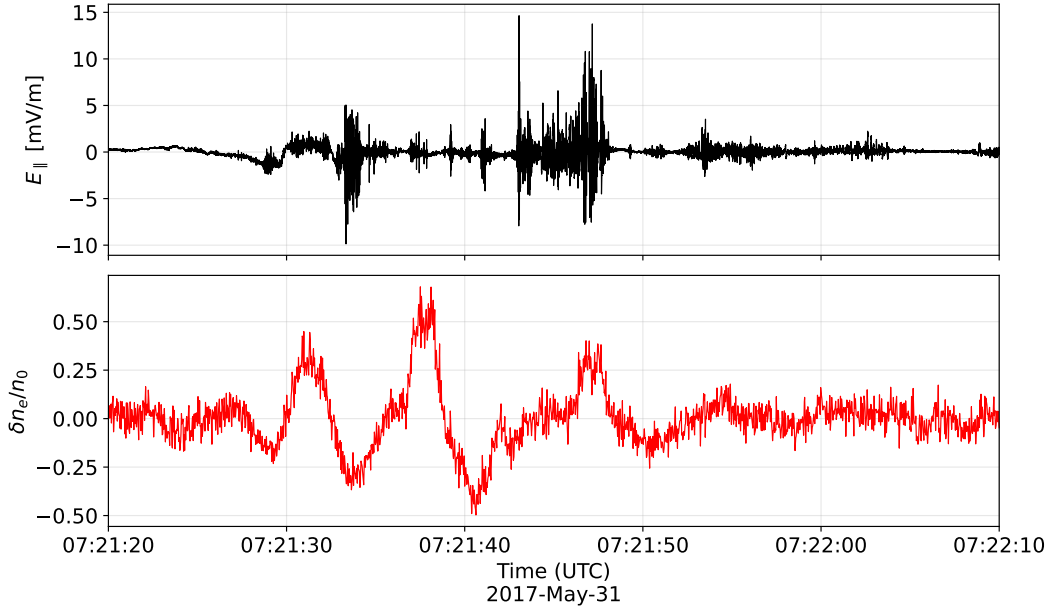


Figure 5: Parallel electric field and density structuring during the analysis interval. Top: $E_{\parallel} = \mathbf{E} \cdot \mathbf{B}/|\mathbf{B}|$, computed by interpolating \mathbf{B} to the electric-field timeline and projecting \mathbf{E} along $\hat{\mathbf{b}}$. Bottom: normalized density fluctuation $\delta n_e/n_0$, with n_0 defined as an 8-s moving-average background. The interval contains intense, intermittent E_{\parallel} excursions (peaks approaching ~ 15 mV/m) together with large density perturbations (enhancements up to order ~ 0.6 and depletions down to order ~ -0.5 in $\delta n_e/n_0$). A zero-lag Pearson correlation computed over 07:21:30–07:21:45 UTC gives $r = -0.03$, indicating no simple linear, zero-lag association between the instantaneous signed E_{\parallel} waveform and the smoothed density fluctuation under the adopted filtering and time-base choices.

cadence-matched measures of $|E_{\parallel}|$ or band-limited analysis) when assessing the detailed coupling between non-ideal fields and compressive plasma response.

4.7. Energy Conversion Proxies in the Electron Frame

To complement the spectral and correlation diagnostics, a cadence-matched proxy for local field–particle energy exchange is evaluated using the standard work density measures $J_{\parallel} E_{\parallel}$ and $\mathbf{J} \cdot \mathbf{E}'$. Here,

$$\mathbf{J}(t) = e n_e(t) [\mathbf{V}_i(t) - \mathbf{V}_e(t)], \quad (5)$$

is obtained from MMS/FPI ion and electron bulk moments, and the electron-frame electric field is

$$\mathbf{E}'(t) = \mathbf{E}(t) + \mathbf{V}_e(t) \times \mathbf{B}(t). \quad (6)$$

All quantities are evaluated on the ion-moment time base: \mathbf{E} (EDP) and \mathbf{B} (FGM) are linearly interpolated to the ion-moment timestamps prior to computing $\hat{\mathbf{b}} = \mathbf{B}/|\mathbf{B}|$, $E_{\parallel} = \mathbf{E} \cdot \hat{\mathbf{b}}$, and $J_{\parallel} = \mathbf{J} \cdot \hat{\mathbf{b}}$. This cadence-matching is required for a physically consistent product and naturally suppresses the narrowest E_{\parallel} spikes that are visible at the native EDP sampling in the overview figure.

Figure 6 summarizes the resulting time series over 07:21:15–07:22:10 UTC. Intermittent E_{\parallel} excursions coincide with enhanced J_{\parallel} variability, and the corresponding work density proxies show bursty excursions of order 10^{-1} nW/m³. The two measures, $J_{\parallel} E_{\parallel}$ and $\mathbf{J} \cdot \mathbf{E}'$, track each other closely for much of the interval, indicating that on the moment cadence the inferred energy exchange is largely accounted for by the field-aligned contribution. The sign changes in both proxies indicate that the estimate represents local energy exchange rather than a guaranteed net heating rate; it is therefore used here as a conservative indicator of when and where strong field–particle coupling is occurring during the wave-active interval.

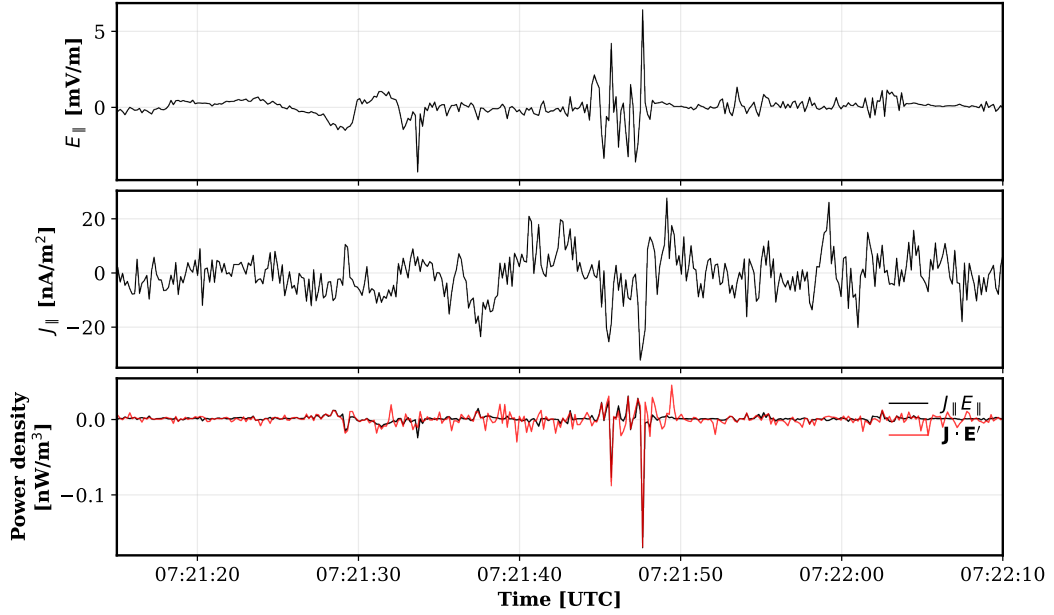


Figure 6: Cadence-matched energy-conversion proxies during 2017-05-31/07:21:15–07:22:10 UTC. Top: signed $E_{\parallel} = \mathbf{E} \cdot \hat{\mathbf{b}}$ evaluated on the ion-moment time base after interpolating EDP \mathbf{E} and FGM \mathbf{B} to the moment timestamps. Middle: J_{\parallel} from moments, using $\mathbf{J} = en_e(\mathbf{V}_i - \mathbf{V}_e)$. Bottom: work density proxies $J_{\parallel}E_{\parallel}$ (black) and $\mathbf{J} \cdot \mathbf{E}'$ (red), where $\mathbf{E}' = \mathbf{E} + \mathbf{V}_e \times \mathbf{B}$. The bursty excursions (both signs) provide a time-domain proxy for intervals of enhanced field–particle energy exchange on the moment cadence.

5. Discussion

5.1. Evidence for KAW Turbulence in the Outer PSBL

The observations presented here provide multiple lines of evidence that KAW turbulence is active in the outer PSBL/lobe boundary region. First, the electric-to-magnetic field ratio $\mathcal{R} = 2.5 \pm 1.2$ significantly exceeds the MHD Alfvén wave value of unity, consistent with the theoretical expectation for KAWs at $k_{\perp} \rho_i \gtrsim 1$ (Stasiewicz et al., 2000; Chaston et al., 2008). Second, the magnetic fluctuations exhibit strong perpendicular anisotropy ($|\delta B_{\perp}|^2 \gg |\delta B_{\parallel}|^2$), a defining characteristic of KAWs that distinguishes them from fast magnetosonic modes or mirror mode structures (Gary, 1986; Sahraoui et al., 2012). Third, the spectral break near the ion cyclotron frequency marks the transition from MHD to kinetic physics, as expected when the turbulent cascade reaches ion gyroscale wavelengths. Fourth, the magnetic compressibility $C_{\parallel} \approx 0.03$ in the kinetic range (Figure 3) falls well below both the isotropic value (1/3) and the empirical KAW threshold (~ 0.1), providing quantitative confirmation that the fluctuations are predominantly transverse. This low compressibility is inconsistent with mirror modes ($C_{\parallel} \sim 0.5\text{--}1$) or fast magnetosonic turbulence, further supporting the KAW interpretation.

These findings extend previous observations of KAW turbulence in the central PSBL (Wygant et al., 2002; Chaston et al., 2008) to the cooler outer PSBL adjacent to the magnetotail lobes. The relatively low ion temperature ($T_i = 0.65 \pm 0.55$ keV) compared to the typical PSBL values of 1–5 keV suggests that our event captures the transition region where lobe plasma mixes with plasma sheet particles. Despite these cooler conditions, KAW turbulence remains active, indicating that kinetic-scale energy dissipation may operate across a broader range of magnetotail environments than previously documented.

5.2. Parallel Electric Field Structures and Identification of Dissipation Pathway

The overview time series shows brief, high-cadence enhancements in $|\delta E_{\parallel}|$ approaching 13–15 mV/m (Figure 2c). In the cadence-matched energy-conversion analysis, E_{\parallel} is evaluated on the ion-moment time base, so the narrowest spikes visible at the native EDP cadence are strongly suppressed (Figure 6). The strongly intermittent morphology and the sub-spin timescales are consistent with localized non-ideal structures (e.g., solitary electric-field structures

or phase-steepened packets) embedded within the KAW turbulence, rather than with a purely sinusoidal linear KAW waveform.

Parallel electric fields of this magnitude have the potential to accelerate electrons along the magnetic field direction. For reference, the electron thermal velocity at $T_e = 0.27$ keV is $v_{th,e} \approx 9700$ km/s, and order-of-magnitude estimates suggest energy gains $\Delta W \sim eE_{\parallel}L$ could range from tens of eV to keV scales depending on the parallel coherence length L of the structures. However, such estimates require validation through electron pitch-angle distribution analysis to identify field-aligned acceleration signatures and multi-spacecraft timing to constrain structure scales. Without this supporting evidence, the electron energization implications of these E_{\parallel} observations remain provisional.

The near-zero Pearson correlation between the instantaneous signed E_{\parallel} waveform and the background-removed density fluctuation ($r = -0.03$) indicates that, under the adopted filtering and time-base choices, there is no evidence for a simple linear, zero-lag correspondence between these two quantities. This result does not exclude time-lagged or nonlinear coupling, nor does it rule out scale-dependent relationships, but it argues against an interpretation in which the largest E_{\parallel} spikes are merely proportional to the moment-scale density enhancement/depletion captured by the 8-s background. Taken together with the bursty $J_{\parallel}E_{\parallel}$ and $\mathbf{J} \cdot \mathbf{E}'$ signatures, the observations are consistent with localized wave-particle energy exchange occurring within a strongly structured boundary-layer plasma. A specific damping channel (e.g., electron Landau damping) is plausible but is not uniquely constrained by the present field-moment diagnostics.

5.3. Steep Spectral Slope and Enhanced Dissipation

The measured kinetic range power density spectral slope of $\alpha = -3.48 \pm 0.13$ is steeper than theoretical predictions for undamped KAW turbulence. The observed slope is similar to the $\alpha \approx -3$ to -4 values reported in other magnetospheric and solar wind KAW studies where strong damping is inferred (Sahraoui et al., 2009; Alexandrova, Lacombe, Mangeney, Grappin and Maksimovic, 2012; Huang et al., 2014), supporting the interpretation that the turbulence in this event is dissipating efficiently at kinetic scales. Several factors may contribute to this steepening:

Landau damping: In a plasma with $T_i/T_e \approx 2.4$, electron Landau damping of KAWs is expected to be significant at sub-ion scales where $k_{\parallel}v_{th,e} \sim \omega$ (Howes, Cowley, Dorland, Hammett, Quataert and Schekochihin, 2006; Schekochihin, Cowley, Dorland, Hammett, Howes, Quataert and Tatsuno, 2009). The damping rate increases with $k_{\perp}\rho_i$, progressively removing energy from the cascade and steepening the spectrum beyond passive cascade predictions. This effect has been demonstrated numerically by Chettri et al. (2025), who showed that including phenomenological Landau damping in a modified nonlinear Schrödinger equation steepens the sub-ion range spectrum from $k_{\perp}^{-8/3}$ to $k_{\perp}^{-11/3}$ in magnetosheath-like conditions.

Ion Landau damping of compressive fluctuations: The relatively high T_i/T_e ratio suppresses freely propagating ion acoustic modes, but in a strongly structured boundary-layer plasma, compressive responses can still be continuously driven by finite-amplitude Alfvénic/KAW fluctuations. The co-occurrence of large density variability with the wave-active interval (Figure 5) is compatible with such coupling, although the present correlation test does not show a simple linear, zero-lag correspondence between the instantaneous signed E_{\parallel} waveform and the background-removed density fluctuation. In this case, any compressive energy injected into ion-acoustic-like responses would be expected to be strongly damped, providing an additional route for energy removal that is not captured in idealized undamped KAW cascade theories (Terradas et al., 2022; Verscharen et al., 2024).

Intermittency: Turbulent dissipation concentrated in localized current sheets and coherent structures produces steeper spectral slopes than homogeneous cascade models (Osman, Wan, Matthaeus, Breech and Oughton, 2011; Greco, Perri, Servidio, Yordanova and Veltri, 2012). The impulsive nature of the E_{\parallel} signatures in Figure 2(c) is consistent with intermittent energy dissipation.

5.4. Limitations and Caveats

Single event: This study analyzes a single 50-second interval during one PSBL crossing. Statistical studies across multiple events are needed to assess how representative these observations are of outer PSBL conditions generally.

Short interval duration: The 50-second analysis window limits the low-frequency extent of reliable spectral estimates. We therefore do not characterize the MHD inertial range slope or the complete turbulent cascade from injection to dissipation scales.

Validity of the Taylor hypothesis: The observed bulk ion velocity ($|\mathbf{V}_i| \approx 150$ km/s, corresponding to $|\mathbf{V}_i|/v_A \approx 0.23$) does not satisfy the standard condition $|\mathbf{V}_{flow}| \gg v_A$ required for a strict Taylor hypothesis mapping between temporal frequency and spatial wavenumber. However, at kinetic scales ($k_{\perp}\rho_i \gtrsim 1$), the dispersive nature of kinetic

Alfvén waves reduces the phase speed relative to v_A , which can improve the applicability of the hypothesis at the smallest scales considered (Howes, Klein and TenBerge, 2014). Even with this mitigation, the low flow speed introduces systematic uncertainties: spectral indices may be biased by $\Delta\alpha \approx \pm 0.3$ – 0.5 , and wavenumber estimates by a factor of ~ 2 (Klein, Howes, TenBerge and Podesta, 2014). At sub-ion scales, kinetic Alfvén wave dispersion and anisotropy further complicate a direct frequency–wavenumber interpretation, so the reported kinetic-range slope should be regarded as a frequency-domain characterization of the scaling. Importantly, our identification of KAW turbulence relies primarily on the electric-to-magnetic field ratio and magnetic compressibility, which do not require frequency-to-wavenumber conversion. Consequently, spectral indices are interpreted with appropriate systematic uncertainty.

Particle distribution analysis: Direct verification of electron Landau damping would require detailed analysis of electron velocity distributions to identify resonant signatures such as flattening near the parallel phase velocity. While the FPI instrument provides such data, this analysis will be carried out in future work.

6. Conclusions

We have presented MMS observations of kinetic Alfvén wave turbulence during a PSBL crossing on May 31, 2017. The principal findings are:

1. **KAW identification:** The electromagnetic fluctuations exhibit properties consistent with KAW turbulence, including (i) an electric-to-magnetic field ratio $\mathcal{R} = 2.5 \pm 1.2$ exceeding the MHD limit; (ii) strong perpendicular magnetic anisotropy ($|\delta B_{\perp}|^2 \gg |\delta B_{\parallel}|^2$); (iii) low magnetic compressibility in the kinetic range ($C_{\parallel} \approx 0.03$); and (iv) a spectral break near the ion cyclotron frequency ($f_{ci} \approx 0.18$ Hz).
2. **Steep kinetic-range spectrum:** The perpendicular magnetic spectrum in the kinetic range follows a power law with slope $\alpha = -3.48 \pm 0.13$, steeper than undamped KAW cascade predictions ($-7/3$ to $-8/3$), consistent with substantial energy removal from the cascade at sub-ion scales.
3. **Parallel fields and density structuring:** Impulsive E_{\parallel} structures reach 13–15 mV/m and large-amplitude density fluctuations occur during the wave-active interval ($\delta n/n$ up to $\sim 68\%$). A zero-lag Pearson correlation computed between the instantaneous signed E_{\parallel} waveform and the background-removed density fluctuation gives $r = -0.03$, indicating no simple linear, zero-lag correspondence under the adopted processing choices. Together with the bursty $J_{\parallel} E_{\parallel}$ and $\mathbf{J} \cdot \mathbf{E}'$ proxies, these observations are consistent with localized field–particle energy exchange within a strongly structured boundary-layer plasma; a specific damping channel (e.g., Landau damping) is plausible but is not uniquely constrained by the present diagnostics.
4. **Outer PSBL regime:** The event occurs in a relatively cold, outer PSBL/lobe boundary environment ($T_i \approx 0.65$ keV, $\beta_i \approx 0.29$), extending KAW turbulence observations to the cooler edge of the plasma sheet boundary layer.

Future work will include particle distribution analyses to test for resonant signatures, multi-spacecraft timing to constrain structure scales and wavevector properties, and surveys across multiple PSBL crossings to assess the prevalence of KAW turbulence and associated kinetic-scale energy conversion in this region.

Data Availability Statement

The observational data from the Magnetospheric Multiscale (MMS) mission used in this study are publicly available from the NASA Space Physics Data Facility (<https://spdf.gsfc.nasa.gov/pub/data/mms/>). Specifically, we use MMS1 Level-2 burst-mode data products: FGM magnetic field (mms1_fgm_brst_l2), EDP electric field (mms1_edp_brst_l2), and FPI ion/electron moments (mms1_dis_brst_l2, mms1_des_brst_l2) for the interval 2017-05-31 07:21:00–07:22:20 UTC. Data were accessed and processed using the PYSPEDAS software package. The analysis scripts used to generate the figures in this work are available from the corresponding author upon reasonable request.

Declaration of Competing Interest

The authors declare that they have no known competing financial interests or personal relationships that could have appeared to influence the work reported in this paper.

Acknowledgments

The author MKC is grateful to the University Grants Commission (UGC), India, for providing financial support through the Non-NET Fellowship. We acknowledge the MMS mission and instrument teams for providing the data used in this study. We particularly thank the FGM, EDP, and FPI teams for their efforts in producing high-quality burst-mode data products.

CRedit authorship contribution statement

Mani K Chettri: Conceptualization, Software, Data curation, Formal analysis, Visualization, Writing – Original draft. **Hemam D. Singh:** Conceptualization, Supervision, Methodology, Validation, Writing – Review & editing. **Rupak Mukherjee:** Supervision, Resources, Writing – Review & editing.

References

- Alexandrova, O., Lacombe, C., Mangeney, A., Grappin, R., Maksimovic, M., 2012. Solar wind turbulent spectrum at plasma kinetic scales. *The Astrophysical Journal* 760, 121.
- Angelopoulos, V., Cruce, P., Drozdov, A., Grimes, E.W., Hatzigeorgiu, N., King, D.A., Larson, D., Lewis, J.W., McTiernan, J.M., Roberts, D.A., Russell, C.L., Hori, T., Kasahara, Y., Kumamoto, A., Matsuoka, A., Miyashita, Y., Miyoshi, Y., Shinohara, I., Teramoto, M., Faden, J.B., Halford, A.J., McCarthy, M., Millan, R.M., Sample, J.G., Smith, D.M., Woodger, L.A., Bonnell, J.W., Loto'aniu, T.M., Reno, M.A., Singer, H.J., 2019. The space physics environment data analysis system (SPEDAS). *Space Science Reviews* 215, 9.
- Baumjohann, W., Paschmann, G., Cattell, C.A., 1988. Average plasma properties in the central plasma sheet. *Journal of Geophysical Research: Space Physics* 93, 11507–11520.
- Boldyrev, S., Perez, J.C., 2012. Spectrum of kinetic-Alfvén turbulence. *The Astrophysical Journal Letters* 758, L44.
- Burch, J.L., Moore, T.E., Torbert, R.B., Giles, B.L., 2016. Magnetospheric Multiscale overview and science objectives. *Space Science Reviews* 199, 5–21.
- Chaston, C.C., Bonnell, J.W., McFadden, J.P., Carlson, C.W., Cully, C., Le Contel, O., Roux, A., Auster, H.U., Glassmeier, K.H., Angelopoulos, V., Russell, C.T., 2008. Turbulent heating and cross-field transport near the magnetopause from THEMIS. *Geophysical Research Letters* 35, L17S08.
- Chen, C.H.K., Klein, K.G., Howes, G.G., 2019. Evidence for electron Landau damping in space plasma turbulence. *Nature Communications* 10, 740.
- Chen, F.F., 1984. *Introduction to Plasma Physics and Controlled Fusion*. 2nd ed., Plenum Press, New York.
- Chettri, M.K., Singh, H.D., Shrivastav, V., Singh, B., Mukherjee, R., 2025. Damped kinetic Alfvén waves in earth's magnetosheath: Numerical simulations and mms observations. *arXiv preprint arXiv:2512.09828*.
- Eastman, T.E., Frank, L.A., Peterson, W.K., Lennartsson, W., 1984. The plasma sheet boundary layer. *Journal of Geophysical Research: Space Physics* 89, 1553–1572.
- Ergun, R.E., Goodrich, K.A., Stawarz, J.E., Andersson, L., Angelopoulos, V., 2015. Large-amplitude electric fields associated with bursty bulk flow braking in the Earth's plasma sheet. *Journal of Geophysical Research: Space Physics* 120, 1832–1844.
- Ergun, R.E., Tucker, S., Westfall, J., Goodrich, K.A., Malaspina, D.M., Summers, D., Wallace, J., Karlsson, M., Mack, J., Brennan, N., Pyber, B., Withnell, P., Torbert, R., Macri, J., Rau, D., Dors, I., Needell, J., Lindqvist, P.A., Olsson, G., Cully, C.M., 2016. The axial double probe and fields signal processing for the MMS mission. *Space Science Reviews* 199, 167–188.
- Gary, S.P., 1986. Low-frequency waves in a high-beta collisionless plasma: polarization, compressibility and helicity. *Journal of Plasma Physics* 35, 431–447.
- Gershman, D.J., F-Viñas, A., Dorelli, J.C., Boardsen, S.A., Avakov, L.A., Bellan, P.M., Schwartz, S.J., Lavraud, B., Coffey, V.N., Chandler, M.O., Saito, Y., Paterson, W.R., Fuselier, S.A., Ergun, R.E., Strangeway, R.J., Russell, C.T., Giles, B.L., Pollock, C.J., Torbert, R.B., Burch, J.L., 2017. Wave-particle energy exchange directly observed in a kinetic Alfvén-branch wave. *Nature Communications* 8, 14719.
- Greco, A., Perri, S., Servidio, S., Yordanova, E., Veltri, P., 2012. The complex structure of magnetic field discontinuities in the turbulent solar wind. *The Astrophysical Journal Letters* 749, L39.
- Hasegawa, A., Chen, L., 1976a. Kinetic processes in plasma heating by resonant mode conversion of Alfvén wave. *Physics of Fluids* 19, 1924–1934.
- Hasegawa, A., Chen, L., 1976b. Parametric decay of “kinetic Alfvén wave” and its application to plasma heating. *Physical Review Letters* 36, 1362–1365.
- Howes, G.G., Cowley, S.C., Dorland, W., Hammitt, G.W., Quataert, E., Schekochihin, A.A., 2006. Astrophysical gyrokinetics: basic equations and linear theory. *The Astrophysical Journal* 651, 590–614.
- Howes, G.G., Cowley, S.C., Dorland, W., Hammitt, G.W., Quataert, E., Schekochihin, A.A., 2008. A model of turbulence in magnetized plasmas: implications for the dissipation range in the solar wind. *Journal of Geophysical Research: Space Physics* 113, A05103.
- Howes, G.G., Klein, K.G., TenBarge, J.M., 2014. Validity of the Taylor hypothesis for linear kinetic waves in the weakly collisional solar wind. *The Astrophysical Journal* 789, 106.
- Huang, S.Y., Sahraoui, F., Deng, X.H., He, J.S., Yuan, Z.G., Zhou, M., Pang, Y., Fu, H.S., 2014. Kinetic turbulence in the terrestrial magnetosheath: Cluster observations. *The Astrophysical Journal Letters* 789, L28.
- Klein, K.G., Howes, G.G., TenBarge, J.M., Podesta, J.J., 2014. Physical interpretation of the angle-dependent magnetic helicity spectrum in the solar wind: The necessity of multipoint measurements. *The Astrophysical Journal* 785, 138.

- Lindqvist, P.A., Olsson, G., Torbert, R.B., King, B., Granoff, M., Rau, D., Needell, G., Turco, S., Dors, I., Beckman, P., Macri, J., Frost, C., Salwen, J., Eriksson, A., Ahlen, L., Khotyaintsev, Y.V., Porter, J., Lappalainen, K., Ergun, R.E., Wimmer, W., Tucker, S., 2016. The spin-plane double probe electric field instrument for MMS. *Space Science Reviews* 199, 137–165.
- Lysak, R.L., Lotko, W., 1996. Magnetosphere-ionosphere coupling by Alfvén waves at midlatitudes. *Journal of Geophysical Research: Space Physics* 101, 5085–5094.
- Osman, K.T., Wan, M., Matthaeus, W.H., Breech, B., Oughton, S., 2011. Directional alignment and non-Gaussian statistics in solar wind turbulence. *The Astrophysical Journal Letters* 741, L19.
- Pollock, C., Moore, T., Jacques, A., Burch, J., Gliese, U., Saito, Y., Ombert, T., Avranov, L., Barber, A., Coffey, V., Dorelli, J., Gershman, D., Giles, B., Rosnack, T., Sber, C., Tucker, S., Westlake, J., Young, D., et al., 2016. Fast plasma investigation for Magnetospheric Multiscale. *Space Science Reviews* 199, 331–406.
- Roberts, O.W., Narita, Y., Escoubet, C.P., 2017. Direct measurement of anisotropic and asymmetric wave vector spectrum in ion-scale solar wind turbulence. *The Astrophysical Journal Letters* 851, L11.
- Russell, C.T., Anderson, B.J., Baumjohann, W., Bromund, K.R., Dearborn, D., Fischer, D., Le, G., Leinweber, H.K., Leneman, D., Magnes, W., Means, J.D., Moldwin, M.B., Nakamura, R., Pierce, D., Plaschke, F., Rowe, K.M., Slavin, J.A., Strangeway, R.J., Torbert, R.B., Hagen, C., Jerber, I., Valavanoglou, A., Richter, I., 2016. The Magnetospheric Multiscale magnetometers. *Space Science Reviews* 199, 189–256.
- Sahraoui, F., Belmont, G., Goldstein, M.L., 2012. New insight into short-wavelength solar wind fluctuations from Vlasov theory. *The Astrophysical Journal* 748, 100.
- Sahraoui, F., Goldstein, M.L., Robert, P., Khotyaintsev, Y.V., 2009. Evidence of a cascade and dissipation of solar-wind turbulence at the electron gyroscale. *Physical Review Letters* 102, 231102.
- Schekochihin, A.A., Cowley, S.C., Dorland, W., Hammett, G.W., Howes, G.G., Quataert, E., Tatsuno, T., 2009. Astrophysical gyrokinetics: kinetic and fluid turbulent cascades in magnetized weakly collisional plasmas. *The Astrophysical Journal Supplement Series* 182, 310–377.
- Stasiewicz, K., Bellan, P., Chaston, C., Kletzing, C., Lysak, R., Maggs, J., Pokhotelov, O., Seyler, C., Shukla, P., Stenflo, L., Streltsov, A., Wahlund, J.E., 2000. Small scale Alfvénic structure in the aurora. *Space Science Reviews* 92, 423–533.
- Stawarz, J.E., Ergun, R.E., Goodrich, K.A., 2017. Generation of high-frequency electric field activity by turbulence in the Earth's magnetotail. *Journal of Geophysical Research: Space Physics* 122, 1512–1533.
- Terradas, J., Soler, R., Oliver, R., Ballester, J.L., 2022. Parametric decay of standing Alfvén waves in a coronal loop. *Astronomy & Astrophysics* 660, A136.
- Torrence, C., Compo, G.P., 1998. A practical guide to wavelet analysis. *Bulletin of the American Meteorological Society* 79, 61–78.
- Verscharen, D., Chandran, B.D.G., Jeong, S.Y., et al., 2024. Parametric decay instability of circularly polarised Alfvén waves with a spectrum of wavevectors: 3D hybrid simulations. *arXiv preprint ArXiv:2403.08179 [physics.space-ph]*.
- Voitenko, Y., Goossens, M., 1998. Excitation of kinetic Alfvén turbulence by MHD waves and energization of space plasmas. *Nonlinear Processes in Geophysics* 5, 1–12.
- Wygant, J.R., Keiling, A., Cattell, C.A., Lysak, R.L., Temerin, M., Mozer, F.S., Kletzing, C.A., Scudder, J.D., Streltsov, V., Lotko, W., Russell, C.T., 2002. Evidence for kinetic Alfvén waves and parallel electron energization at 4–6 R_E altitudes in the plasma sheet boundary layer. *Journal of Geophysical Research: Space Physics* 107, 1201.
- Zhang, Z., Yuan, Z., Huang, S., Yu, X., Xue, Z., Deng, D., Huang, Z., 2022. Observations of kinetic Alfvén waves and associated electron acceleration in the plasma sheet boundary layer. *Earth and Planetary Physics* 6, 465–473.